




Shockley-Read-Hall recombination and trap levels in $\text{In}_{0.53}\text{Ga}_{0.47}\text{As}$ point defects from first principles

Christian Dam Vedel ^{1,2,*}, Tue Gunst ², Søren Smidstrup,² and Vihar P. Georgiev ¹

¹*Device Modelling Group, James Watt School of Engineering, University of Glasgow, Glasgow G12 8QQ, United Kingdom*

²*Synopsys Denmark, Fruebjergvej 3, Postbox 4, DK-2100 Copenhagen, Denmark*



(Received 20 July 2023; revised 1 September 2023; accepted 11 September 2023; published 26 September 2023)

We present charge state transition levels of 23 intrinsic defects and dopant substitutions in the compound III-V semiconductor $\text{In}_{0.53}\text{Ga}_{0.47}\text{As}$, calculated with density functional theory. We also report the Shockley-Read-Hall (SRH) recombination rate and capture coefficients for defects found to have deep trap levels. Our calculations show that seven of the considered defects exhibited deep trap levels capable of acting as electron and hole traps in devices: the $\text{As}_{\text{In}/\text{Ga}}$ antisites, the $\text{V}_{\text{In}/\text{Ga}}$ vacancies, the $(\text{In}/\text{Ga})_{\text{As}}-\text{As}_{\text{In}/\text{Ga}}$ double antisites, and the Sn_{As} substitution. We found that the As_{In} antisite exhibits the highest electron-capture coefficient of $C_n = 2.2 \times 10^{-5} \text{ cm}^3 \text{ s}^{-1}$ at room temperature. The defect with the highest hole-capture coefficient was found to be the $\text{In}_{\text{As}}-\text{As}_{\text{In}}$ double antisite, with $C_p = 3.4 \times 10^{-6} \text{ cm}^3 \text{ s}^{-1}$. Furthermore, this defect also causes the highest recombination rate in the intrinsic semiconductor, owing to its likewise relatively large electron-capture coefficient. The defects which are most likely to occur are argued to be the antisites, due to their low formation energies and matching transition levels with experiments. Additionally, it is found that the Sn_{As} substitution also causes a significant recombination in the semiconductor, but it is argued to only be of importance at very high doping levels.

DOI: [10.1103/PhysRevB.108.094113](https://doi.org/10.1103/PhysRevB.108.094113)

I. INTRODUCTION

III-V materials like InGaAs have features which make them promising candidates to incorporate into multiple devices in fields like microelectronics and photonics. Due to their high carrier mobilities, they can potentially be used as channel materials in metal-oxide semiconductors (MOSs), replacing the conventionally used silicon [1–6]. In the case of III-V compounds like InGaAs, their band gap can be tuned by varying the mole fraction of the constituents. Even the nature of the band gap can be changed, from direct to indirect, in certain compounds [7,8]. These features make III-V compounds immensely important for photonic applications [9], such as in lasers [10,11] and detectors [12,13].

Despite these attractive features, III-V's have yet to be widely industrially adopted. The reason for this can be found in the interfaces between III-V's and oxides. Whereas silicon has a stable and simple oxide (SiO_2), III-V's lack such a high-quality intrinsic passivation oxide. The poor quality of III-V/oxide interfaces causes surface strain and imperfect passivation, which leads to large interface state densities from native defects, which in turn decrease device performance [14–17]. For solar cells, the interface states cause light carrier loss [18], for lasers the emission efficiency is decreased [19], and for MOS field-effect transistors (MOSFETs), the interface

states cause C-V dispersion and hysteresis [20,21]. Multiple methods have been developed to improve the interface quality and reduce the number of defects, such as additional passivation film deposition, sulfur passivation, plasma passivation, and temperature annealing [22,23]. Despite great progress in this field, a complete solution which adequately removes the defects has yet to be found.

In recent work, the origin of the experimentally measured interface state densities has been suggested [24,25]. This is done by comparing the interface state densities of III-V compounds with various oxides and passivation techniques, to accurate first-principles calculations of defects. It is hypothesized that the III-V/oxide interfaces' strain relaxation induce native bulk defects below the interfaces in the III-V semiconductors, such as vacancies and antisites, on top of forming dangling bonds at the interface [26,27]. This explains the limited success of the various passivation methods, as most methods simply passivate the dangling bonds at the interface. To further the III-V adaptation progress, understanding the exact nature of the interface state densities is crucial to guide the continued passivation research efforts.

In this paper, we will investigate 23 different point defects in InGaAs, in order to shed more light on the origin of the III-V/oxide interface state densities. We will calculate the transition levels of both intrinsic defects, as well as substitutions with dopants commonly used in InGaAs growth procedures. $\text{In}_{0.53}\text{Ga}_{0.47}\text{As}$ is chosen specifically due to its high electron mobility and its lattice match with InP, which makes it ideal for photonic applications such as p-InP/i-InGaAs/n-InP (PIN) photodetectors [28].

One defect-derived effect, limiting the performance of PIN devices is the Shockley-Read-Hall (SRH) recombination. SRH recombination is a nonradiative process, in which

*christianvedel@hotmail.com

excited carriers are trapped by a defect with a deep trap level, wherein they recombine by emitting phonons [29]. To evaluate the studied defects' detrimental impact on device properties, we will therefore additionally calculate this SRH recombination.

II. METHODS

For our simulations we use the first-principles method density functional theory (DFT), as implemented in the U-2022.12 version of the state-of-the-art simulation software suite QUANTUMATK by Synopsys [30]. Atoms are treated explicitly by linear combination of atomic orbitals (LCAO) basis sets and their corresponding pseudopotential. We used the “medium” version of the PSEUDODOJO basis set [31], together with a Brillouin zone sampling density of 6 \AA and a density mesh cutoff of 105 Ha. For the occupation smearing function we used a Fermi-Dirac distribution at 300 K. All investigated systems were relaxed, until the forces between the atoms were smaller than 0.05 eV/\AA . For the pristine systems, we also relaxed the cubic unit cell, until the stress was lower than 0.1 GPa. For the exchange correlation, we used the hybrid functional developed by Heyd, Scuseria, and Ernzerhof (HSE06) [32] in all calculations, including relaxations. HSE06 is an improvement of the generalized gradient approximation (GGA) functional developed by Perdew, Burke, and Ernzerhof (PBE) [33], in which a fraction of exact Fock exchange is mixed in. We used the original default fraction of $\frac{1}{4}$ th exact exchange. The reason that we opted for the more computationally expensive HSE06 functional over regular PBE is that studies have shown the necessity of having a good description of the band gap and excited states, when calculating transition levels [34,35]. To lessen the computational burden when using HSE06, we used the auxiliary density matrix method (ADMM) [36], in which a smaller basis set is used for the exchange part of the DFT calculation.

The formation energies of the charged defects, which are needed for the transition levels, are calculated from the DFT calculations as

$$E_f^q = E^{\text{def},q} + E_q^{\text{latt}} - E^{\text{bulk},q} - \sum_i \Delta n_i \mu_i + q(\mu_e^{\text{ref}} - \Delta V_{q/0} + \Delta \mu_e), \quad (1)$$

where $E^{\text{def},q}$ is the total energy of the defect system in the charge state q , $E^{\text{bulk},q}$ is the total energy of the bulk system without the defect, Δn_i is the difference in number of atomic species i in the defect and bulk systems, μ_i is the atomic chemical potential, which we will discuss further later in the paper, μ_e^{ref} is the chemical potential reference level, which will be taken to be the valence band edge, and $\Delta \mu_e$ is the electronic chemical potential relative to it. The terms E_q^{latt} and $\Delta V_{q/0}$ are finite-size correction terms, developed by Freysoldt, Neugebauer, and Van de Walle (FNV) [37–39], to correct for the spurious interaction with the periodic images of the system. The first term corrects for the electrostatic interaction between the charged defects in the periodic images of the supercell, and the second term for the shifting of the bands due to the presence of the defect, in order to align the bands with the neutral bulk. The transition level, sometimes also called the defect level or trap level, is then defined as the electronic

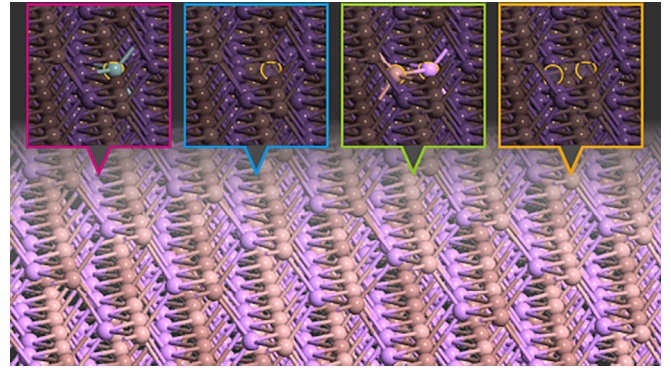


FIG. 1. Atomic structure illustrating the four kinds of point defects studied, embedded in an $\text{In}_{0.53}\text{Ga}_{0.47}\text{As}$ SQS supercell configuration. Illustrations from the left: substitution (purple), vacancy (blue), double antisite (green), and divacancy (orange) point defects.

chemical potential for which the formation energy in Eq. (1) of different charge states coincides.

III. $\text{In}_{0.53}\text{Ga}_{0.47}\text{As}$ STRUCTURE GENERATION

Atomistic simulations of quaternary or ternary compound semiconductors, like $\text{In}_{0.53}\text{Ga}_{0.47}\text{As}$, are more complicated than their binary counterparts, due to the added complexity of handling the random distribution of elements. When considering embedded defects, like we are in this paper, this is complicated even further. Examples of $\text{In}_{0.53}\text{Ga}_{0.47}\text{As}$ structures with embedded defects, of the different types which will be investigated here, are illustrated in Fig. 1.

To accurately model the effect of the random distribution of group III elements in a realistic pristine $\text{In}_{0.53}\text{Ga}_{0.47}\text{As}$ structure, we generate special quasirandom structures (SQS), using an evolutionary method based on the one developed in [40]. The SQS configurations capture the true randomness of the defect-free structure, mimicking the ensemble of many random configurations in the limit of large structures.

Figure 2 summarizes the structure correlation and band gap for increasingly larger supercells and improved settings (specified in the figure caption) for the SQS generation. We search for converged and optimal SQS structures by running the evolutionary algorithm thrice, with increasing accuracy, and compare the spread in correlation function error and band gap of the resulting SQS. Considering the spread and value of the correlation function errors in Fig. 2(a), we find that the supercells consisting of 5 and 6 repetitions of the simple unit cell (250 and 432 atoms) are sufficiently converged with supercell size. The same is seen with the band gaps in Fig. 2(b), where going from 5 to 6 repetitions in the supercell only gets the band gap 10 meV closer to the experimental band gap of 0.74 eV [41]. We also find no improvement when using the higher-accuracy evolutionary algorithm parameters to generate the SQS, illustrating sufficiently converged quasirandom structures.

To further test the generated SQS's, charge state transition levels of an embedded defect are calculated. Charge states depend strongly on the local environment, and could therefore potentially require better converged SQS's than bulk features such as the band gap. We chose to use the As_{In} antisite defect

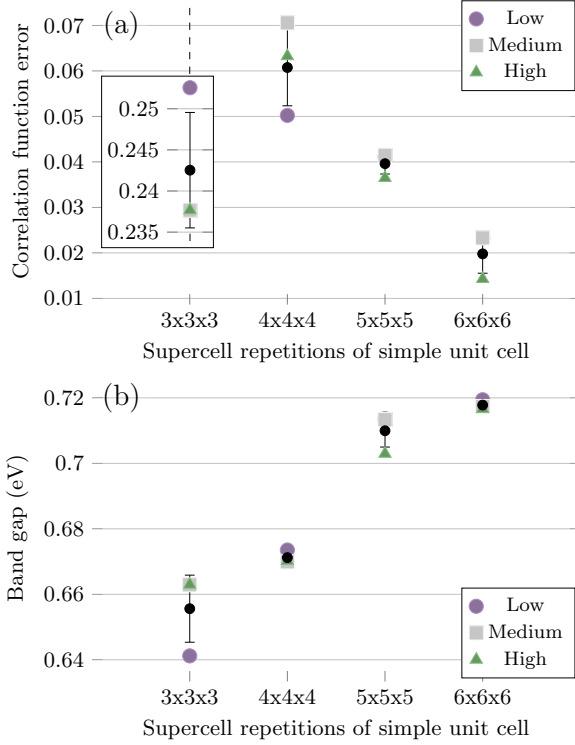


FIG. 2. Special quasirandom structures (SQS) validation of various supercell sizes and evolutionary algorithm parameters. The “low,” “medium,” and “high” set of evolutionary algorithm parameters corresponds to 200, 400, and 600 evolution steps, population sizes of 100, 200, and 300 structures, and 10, 20, and 30 best structures promoted in each step, respectively. The correlation function error of the best structure for each algorithm is shown in (a) and the structures’ band gap in (b), together with the average and standard deviations across the three algorithm runs.

(arsenic replacing an indium atom) for this test since this defect has earlier been proposed to be the most stable of the native defects in $\text{In}_{0.53}\text{Ga}_{0.47}\text{As}$ [24].

Figure 3 shows the obtained transition levels of the antisite in the 5- and 6-repetition SQS supercells. We find that the As_{In} antisite defect has two transition levels in the band gap. These transition levels vary substantially between the different 5-repetition SQS supercells, whereas they exhibit barely any fluctuations in the 6-repetition supercells. It is evident that a larger SQS is required for the investigation of transition levels in defects, as compared to the simulation of bulk properties. Considering the minimal fluctuations of the transition levels in the 6-repetition supercells, we chose to use the “low” SQS of these, as our $\text{In}_{0.53}\text{Ga}_{0.47}\text{As}$ host bulk for our subsequent calculations.

The value of the transition levels shown in Fig. 3, additional transition levels which lie outside of the bulk band gap, as well as the formation energy of the defect in the stable charge state at the chemical potential of the intrinsic neutral bulk, are given in Table III in the Appendix A.

IV. POINT-DEFECT TRAP LEVELS

Using the converged $\text{In}_{0.53}\text{Ga}_{0.47}\text{As}$ SQS configuration, we will embed 23 different experimentally feasible point defects

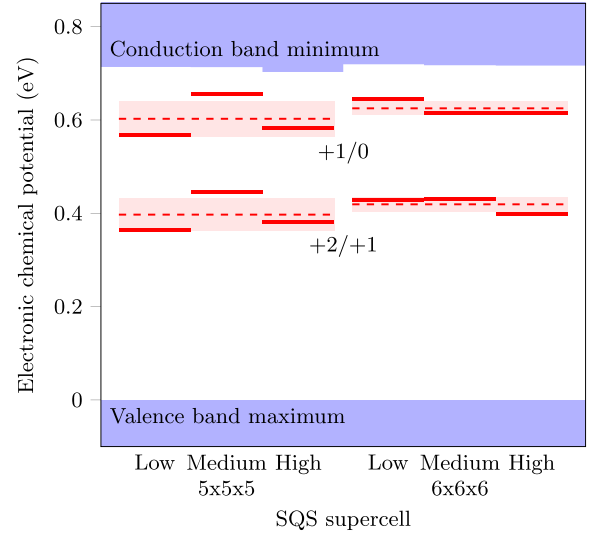


FIG. 3. Transition levels of the As_{In} antisite defect in the SQS $\text{In}_{0.53}\text{Ga}_{0.47}\text{As}$ supercells consisting of $5 \times 5 \times 5$ and $6 \times 6 \times 6$ repetitions of the simple unit cell. The means of the transition levels across the SQS’s resulting from the three different sets of SQS parameters are given by the dashed lines, and the standard deviation by the shaded area. The “low,” “medium,” and “high” labels are explained in the caption in Fig. 2.

and calculate the related transition levels. The 23 point defects can be categorized into four different types (substitutions, vacancies, double antisites, and divacancies), as illustrated in Fig. 1. Specifically, in addition to the As_{In} antisite, we will study the other antisites: As_{Ga} , In_{As} , Ga_{As} , and the double antisites $\text{In}_{\text{As}}-\text{As}_{\text{In}}$, $\text{Ga}_{\text{As}}-\text{As}_{\text{Ga}}$, which are simply the 3-5 elements at two neighboring sites swapped around. We will also investigate the monovacancies V_{In} , V_{Ga} , V_{As} and the divacancies $\text{V}_{\text{As}}-\text{V}_{\text{In}}$, $\text{V}_{\text{As}}-\text{V}_{\text{Ga}}$. The divacancies consist of two vacancies at neighboring 3-5 sites. Finally, we will also look at substitutions with common dopants and contaminants, namely, carbon, tin, zinc, and silicon, substituting any of the bulk species.

We calculated the transition levels close to the stable charge state of all the point defects. Figure 4 shows the results for the defects which exhibited transition levels in the bulk $\text{In}_{0.53}\text{Ga}_{0.47}\text{As}$ band gap. The full list of transition level results is summarized in Table I, together with the formation energy of the defect in its stable charge state. The transition levels with a gray background are not included in Fig. 4.

We see that the formation energy and transition levels of the As_{Ga} antisite are almost identical to those of the As_{In} antisite. This can be explained by the identical local environments on the sites and the chemical similarity between the two species. The same similarity is present between other defects situated either on a gallium or an indium site. The similarity is less prevalent in the case of the In_{As} and Ga_{As} antisites, due to the nearest neighbors being inequivalent. Care was taken to choose an arsenic site, for which the nearest neighbors were 2 of each of gallium and indium, to ensure a more consistent and representative behavior of the point-defect study. To accurately account for the effect of the nearest-neighbor stoichiometry, in principle one should make calculations for

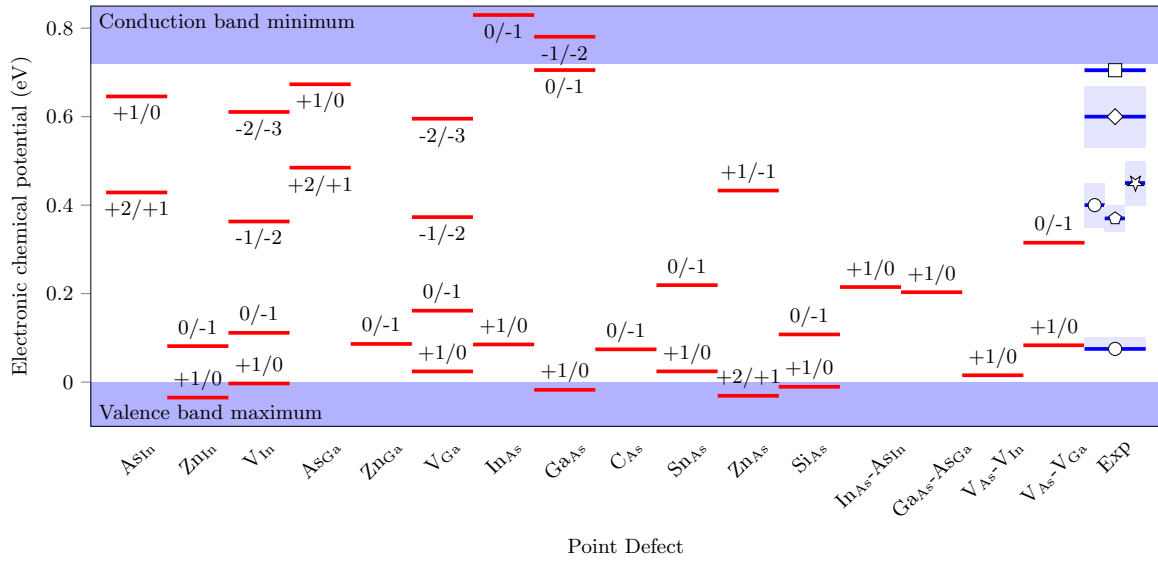


FIG. 4. Transition levels of point defects in $\text{In}_{0.53}\text{Ga}_{0.47}\text{As}$. Only point defects which have a transition level in the band gap are included here. The full study is given in Table I. The experimental transition levels are measured on $\text{In}_{0.53}\text{Ga}_{0.47}\text{As}/\text{oxide}$ interfaces and are determined with various different methods (square [15], diamond [14], circle [26], polygon [27], star [16]). Uncertainties in the experimental values are shown by the blue shaded area.

all types of local environments, and then compute weighted averages according to the fractional occurrences of the local environment in the system. Based on tests on a few of the studied defects, it was found that the effect of this was

TABLE I. Transition levels and formation energies of various point defects in $\text{In}_{0.53}\text{Ga}_{0.47}\text{As}$. The given formation energy is the formation energy of the stable charge state at the chemical potential of the intrinsic neutral bulk. Gray-shaded numbers are transition levels which are not shown in Fig. 4.

(eV)	+3/+2	+2/+1	+1/0	0/-1	-1/-2	-2/-3	E_f
As_{In}	-0.261	0.429	0.646	1.329			2.123
C_{In}		-0.145	0.968	1.221			4.994
Sn_{In}	-0.282	-0.129	1.250	1.535			0.449
Zn_{In}			-0.035	0.081	1.471		0.474
Si_{In}		-0.142	1.222	1.532			0.674
V_{In}			-0.003	0.111	0.363	0.611	4.121
As_{Ga}	-0.251	0.485	0.673	1.348			2.116
C_{Ga}		-0.144	0.995				4.802
Sn_{Ga}		-0.146	1.234				0.525
Zn_{Ga}				0.086	1.503		0.546
Si_{Ga}		-0.147	1.243				0.623
V_{Ga}			0.024	0.161	0.373	0.595	4.108
In_{As}			0.085	0.830	0.948		2.524
Ga_{As}			-0.017	0.705	0.781		2.392
C_{As}				0.074	1.447		3.598
Sn_{As}			0.024	0.219	1.482		1.794
Zn_{As}		-0.031	0.433		1.285		3.038
Si_{As}			-0.011	0.108	1.474		1.641
V_{As}	-0.260	-0.145	0.922				2.667
$\text{In}_{\text{As}}-\text{As}_{\text{In}}$			0.215	1.151			2.921
$\text{Ga}_{\text{As}}-\text{As}_{\text{Ga}}$			0.203	1.141			2.879
$\text{V}_{\text{As}}-\text{V}_{\text{In}}$			0.015	1.003			5.165
$\text{V}_{\text{As}}-\text{V}_{\text{Ga}}$			0.083	0.315			5.056

generally small, which is why it was not studied further and a representative local environment was used instead. As an exception, in the case of the divacancies, the effect of the local environment was more prominent. The large difference between the $0/-1$ transition level of the divacancies likely stems from the difference in the nearest-neighbor species (due to the second vacancy) on the arsenic site. Despite this, the $+1/0$ transition levels and the formation energies are still similar between the divacancies, hinting that the difference could be caused by something else than the local environment of the arsenic site. In the $\text{V}_{\text{As}}-\text{V}_{\text{Ga}}$ divacancy, the defect state associated with the $0/-1$ transition is strongly hybridized with the conduction band state. Because of this, there is a large rearrangement of the bands in the band structure upon the defect levels occupation, which greatly shifts the transition level down in energy.

In the double antisite defects, the same difference on the local environment of the arsenic site appears, but here its effect is negligible. This is likely due to the difference in the interactions in the two types of defects. In the divacancies, the dangling bonds of the uncoordinated indium and gallium sites interact with the dangling bonds of the uncoordinated arsenic sites across the defect. In contrast, there are no dangling bonds in the double antisites; instead there are In-In bonds and Ga-Ga bonds. Despite the double antisite defects being made up of both antisites, their similarity is more akin to the $\text{As}_{\text{In}/\text{Ga}}$ antisites, suggesting that the effect of these is more dominant in the double antisites than the effect of the Ga_{As} and In_{As} antisites.

Comparing the experimentally determined trap level of $\text{In}_{0.53}\text{Ga}_{0.47}\text{As}/\text{oxide}$ interfaces, shown in Fig. 4, with the calculated transition levels, we can attempt to identify the defects. The midgap states align with the $-1/-2$ transitions of the $\text{V}_{\text{In}/\text{Ga}}$ vacancies, the $+1/-1$ transition of the Zn_{As} substitution, and the $+2/+1$ transitions of the $\text{As}_{\text{In}/\text{Ga}}$ antisites. The transition levels close to the conduction band align

with the $-2/-3$ transitions of the $V_{\text{In/Ga}}$ vacancies and the $+1/0$ transitions of the $\text{As}_{\text{In/Ga}}$ antisites for the lower level (diamond) and the $0/-1$ transition of the Ga_{As} antisite for the upper level (square). The transition level close to the valence band aligns with many of the defects, and it has even been shown to align with the As dangling bond [34]. It is noteworthy to notice that it aligns with the $+1/0$ transition in the In_{As} antisite. According to the calculated formation energies shown in Table I, the antisites are the most likely occurring of these defects, with formation energies approximately 2 eV lower than the $V_{\text{In/Ga}}$ vacancies. Additionally, it has been suggested that a charge-compensating effect produces antisites of one kind ($\text{As}_{\text{In/Ga}}$), in response to antisites of the other kind ($[\text{In/Ga}]_{\text{As}}$), in polar materials like InGaAs [42]. From the alignment with calculated transition levels, the calculated defect formation energies and the described compensation rule, the antisites are concluded to be the most likely source of the experimentally observed transition levels. While the double antisites are not detected in experiments, this does not mean that they do not appear. Since they consist of the experimentally found singular antisites, and since their combination is energetically favored over the single antisites, it is reasonable to assume that they also form, albeit possibly in much smaller numbers, owing to the low likelihood of two singular antisites coinciding in space.

Great care should be taken when considering the absolute value of the formation energies reported in Table I. While we have used them to arrive at the conclusion above, they were not used in isolation, but rather as one argument out of several, arriving at the same conclusion. The reported formation energies are the formation energies of the defect configurations, in the charge state which is stable, when the chemical potential is that of the neutral undoped bulk system, as given by Eq. (1). The problem with the definition in Eq. (1) lies with the atomic chemical potential of the added or removed species μ_i of the defect. This chemical potential is taken as the energy per atom of an elemental configuration, in order to have a consistent reference. In a real physical system, however, the species comes from various sources, such as the precursor molecules during growth or the ambient growth atmosphere, rather than an elemental bulk. This unphysical choice of atomic chemical potential, chosen for consistency and simplicity, means that the formation energies should only be considered qualitatively. Since the transition levels are calculated by differences in formation energies, they are not subject to this issue. One qualitative use of the calculated formation energies is the comparison of similar defects to determine which one is more likely than the other, as they all have a common reference. An example of this is the determination of what type of dopants the group IV substitutions are in a III-V material such as $\text{In}_{0.53}\text{Ga}_{0.47}\text{As}$.

It is well known that carbon will act as a p -dopant or a n -dopant, depending on the stoichiometry of the InGaAs compound [43]: this can be determined from the formation energies. In Table I we see that the carbon substitution on the arsenic site has a lower formation energy, of about 1.5 eV, as compared to the indium or gallium sites. Its stable charge state is -1 , meaning it indeed acts as a p -dopant, releasing a hole to the bulk. We also see that there is an upper limit on the doping level that can be achieved using this dopant since if

the chemical potential falls below 0.074 eV above the VBM, the carbon dopants stable charge state will be 0 and it will no longer work as a dopant. Similarly, we find that tin, zinc, and silicon all favor the indium and gallium sites, and that tin and silicon work as good n -dopants, whereas zinc works as a p -dopant with an upper doping level limit of 0.081 eV above the VBM.

It is important to distinguish between “shallow trap levels,” which are transition states close to the band edges, and “deep trap levels,” which lie far above (below) the VBM (CBM). Shallow trap levels work like dopants, depending on the valency of the defect and the charge states involved in the transition level. Deep trap levels act as recombination centers and thus have a detrimental impact on the current conducting properties of the semiconductor. In this work, we partition the transition levels at 0.2 eV ($\approx 8k_B T$ at 300 K) above (below) the VBM (CBM) since defect states associated with transition levels below this threshold hybridize with the valence (conduction) band states and thereby delocalize. Looking at the transition levels in Fig. 4, we see that the $+2/+1$ transition level of the $\text{As}_{\text{In/Ga}}$ antisites ($\approx 9-11k_B T$ below CBM), the $-1/-2$ level of the $V_{\text{In/Ga}}$ vacancies [$\approx 14k_B T$ above (below) VBM (CBM)], the $0/-1$ level of the Sn_{As} substitution ($\approx 8k_B T$ above VBM), the $+1/-1$ level of the Zn_{As} substitution ($\approx 11k_B T$ below CBM), the $+1/0$ level of the double antisites ($\approx 8k_B T$ above VBM) and the $0/-1$ level of the $V_{\text{As}}-V_{\text{Ga}}$ divacancy ($\approx 12k_B T$ above VBM), all exhibit deep trap levels with the chosen partition. To find out how detrimental these specific defects are on the current transport properties of $\text{In}_{0.53}\text{Ga}_{0.47}\text{As}$, we will calculate the trap-assisted recombination rates associated with these deep trap levels.

V. SHOCKLEY-READ-HALL RECOMBINATION

To calculate the SRH recombination capture coefficients, we use the methodology developed by Alkauskas *et al.* [44]. We will briefly outline the main points of the method here. The first step is to replace the complicated real phonon modes, with a single effective phonon mode [45]. This effective phonon mode is chosen as a displacement along the difference in atomic coordinates of the equilibrium configuration, in the initial (excited) state $R_{i:at}$, and the final (ground) state $R_{f:at}$, of the involved charge transition. The generalized configuration coordinate Q along this displacement is then defined as

$$Q^2 = \sum_{\alpha,t} m_{\alpha} (R_{at} - R_{f:at})^2, \quad (2)$$

where m_{α} are atomic masses of atom α and $t = x, y, z$. In this effective coordinate, $Q = 0$ when the atomic configuration is that of the final (ground) state, and $Q = \Delta Q$ when it is that of the initial (excited) state. The frequency of the effective phonon mode in the initial and final charge states are then given by the second-order derivative with regards to the generalized configuration coordinate:

$$\Omega_{i/f}^2 = \frac{\partial^2 E_{i/f}}{\partial Q^2}. \quad (3)$$

A related quantity, the Huang-Rhys factor S , which describes the strength of the electron-phonon interaction, is also calculated from this displacement:

$$S_{i/f} = \frac{1}{2\hbar} (\Delta Q)^2 \Omega_{i/f}. \quad (4)$$

Having reduced the space to a single effective coordinate and phonon mode, the calculation of the electron-phonon coupling in the static and linear-coupling approximation becomes simple:

$$\tilde{W}_{i/f} = \langle \tilde{\psi}_i | \frac{\partial \hat{h}}{\partial Q} | \psi_f \rangle = (\varepsilon_f - \varepsilon_i) \langle \tilde{\psi}_i | \frac{\partial \psi_f}{\partial Q} \rangle, \quad (5)$$

where \hat{h} is the single-particle Hamiltonian of DFT, ε_i is the energy of the single-particle state $\tilde{\psi}_i$, which is the state that corresponds to a hole (electron) in the valence (conduction) band, perturbed by the defect, and ψ_f is the defect state. These single-particle states were identified using electronic inverse participation ratios (IPRs) of the defect systems. Defect states were identified as states with high IPR close to the Fermi level, whereas conduction and valence band states were identified as states with low IPR on either side of the defect state, with energy differences close to the pristine band gap. The calculated electron-phonon coupling is then used with Fermi's golden rule, in order to arrive at the expression for the capture coefficient for the holes and electrons:

$$\begin{aligned} \tilde{C}_{e/h} &= \tilde{V} \frac{2\pi}{\hbar} g \tilde{W}_{i/f}^2 \sum_m w_m \sum_n |\langle \chi_{im} | Q - Q_0 | \chi_{fn} \rangle|^2 \\ &\times \delta(\Delta E + m\hbar\Omega_i - n\hbar\Omega_f). \end{aligned} \quad (6)$$

Here, \tilde{V} is the volume of the supercell, g is the degeneracy of the final state, which is 1 in all cases in this paper, ΔE is the energy difference between the initial and final states, i.e., the trap level, w_m is the thermal occupation of the vibrational state m , and $|\chi_{im/fn}\rangle$ is the ionic wave function of the initial (final) state in vibrational state $m(n)$. Q_0 is the configuration of the starting point for the perturbation theory, i.e., the configuration for which $\tilde{W}_{i/f}$ is calculated. This was chosen to be the initial (excited) state configuration for all transitions since this is the state which captures carriers to the local defect level.

The capture coefficient calculated with Eq. (6) has to be corrected for finite-size effects, caused by the limited size of the supercell:

$$C_{e/h} = f(n, p, T) \tilde{C}_{e/h}. \quad (7)$$

The dimensionless scaling factor $f(n, p, T)$ in Eq. (7) contains both the supercell scaling correction [46] and the Sommerfeld temperature scaling, which corrects for the effect of a charge on the bulk wave function [47].

Using this formalism, as implemented in QUANTUMATK, with the derivatives in Eq. (5) evaluated with finite differences, we calculated the SRH capture coefficients of both electron and hole capture, of all the deep trap levels in Fig. 4, barring the Zn_{As} substitution and the $\text{V}_{\text{As}}\text{-V}_{\text{Ga}}$ divacancy. In both of these two defects, a local single-particle defect state representing the transition could not be clearly distinguished, as they were strongly hybridizing with the valence and conduction

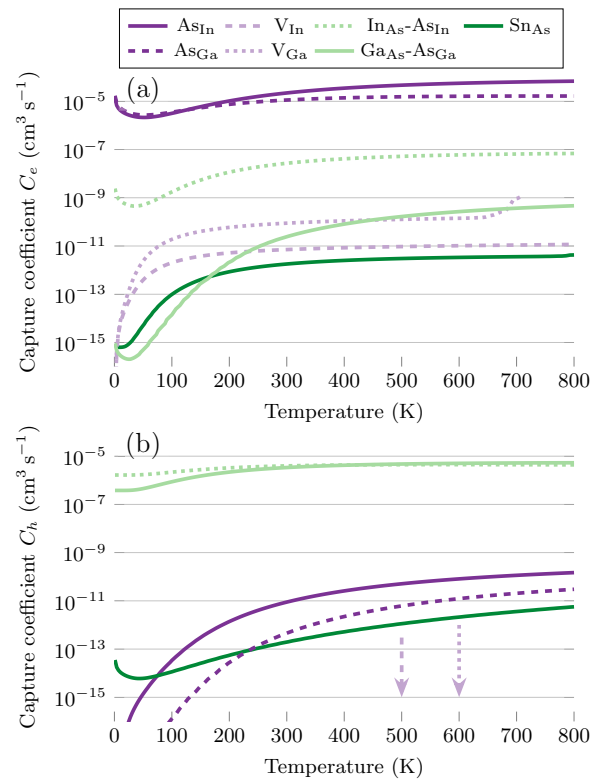


FIG. 5. Shockley-Read-Hall capture coefficients for deep trap levels of point defects in $\text{In}_{0.53}\text{Ga}_{0.47}\text{As}$. (a) Capture of an excited electron in the conduction band. (b) Capture of an excited hole in the valence bands.

bands. The same was also found for most transition levels below the partitioning threshold, thereby confirming our choice of this division. For the hole-capture coefficient, we used the three bulk states, which correspond to the three degenerate valence bands of the $\text{In}_{0.53}\text{Ga}_{0.47}\text{As}$ bulk, as $\tilde{\psi}_i$. The total electron-phonon coupling was then taken as the norm of the three separate electron-phonon matrix elements. For the numeric Sommerfeld scaling function, we used effective masses calculated from fits to the band structure of the $\text{In}_{0.53}\text{Ga}_{0.47}\text{As}$ SQS. The resulting effective masses of $0.33m_0$ and $0.036m_0$ were used for the electron and hole capture, respectively. The resulting capture coefficients can be seen in Fig. 5 as a function of temperature. The hole-capture coefficients of the V_{In} and V_{Ga} vacancies are 7 and 12 orders of magnitude lower than the Sn_{As} substitutions, respectively, and are therefore not shown in the figure.

Due to the exponential scaling of the recombination with the trap level energy, we would expect the vacancies to have the highest average capture coefficients across both electron and hole capture since their trap levels are mid band gap (see Table I). This is not the case, instead the vacancies have capture coefficients many orders of magnitudes below the other defects, for hole capture, and among the lowest of the defects for electron capture. We do, however, see that the antisites have the highest electron capture coefficients, and the double antisites have the highest hole-capture coefficients, in line with their trap levels being closest to the conduction band and valence bands, respectively. Based purely on the

TABLE II. SRH recombination parameters of deep trap levels in $\text{In}_{0.53}\text{Ga}_{0.47}\text{As}$ point defects. The \cdot/\bullet (\bullet/\cdot) symbol refers to the upper (lower) state of the charge transition of the specific defect. The electron-phonon coupling constants are given for all three involved valence band states \tilde{W}_{v1-v3} as well as the conduction band state \tilde{W}_c .

Defect	$\hbar\Omega \cdot/\cdot$ (meV)	$\hbar\Omega \cdot/\bullet$ (meV)	$S \cdot/\cdot$	$S \cdot/\bullet$	ΔQ ($\text{\AA} \text{amu}^{0.5}$)	\tilde{W}_{v1} (eV/ $\text{\AA} \text{amu}^{0.5}$)	\tilde{W}_{v2} (eV/ $\text{\AA} \text{amu}^{0.5}$)	\tilde{W}_{v3} (eV/ $\text{\AA} \text{amu}^{0.5}$)	\tilde{W}_c (eV/ $\text{\AA} \text{amu}^{0.5}$)
As_{In}	17.2	15.5	8.26	7.45	2.01	7.31e-4	6.30e-4	1.22e-5	7.14e-2
As_{Ga}	15.8	14.3	8.08	7.30	2.07	1.84e-4	1.25e-4	1.11e-3	7.15e-2
V_{In}	5.8	16.7	1.52	4.35	1.48	5.73e-3	1.92e-2	1.95e-3	1.63e-4
V_{Ga}	4.6	13.3	1.30	3.74	1.53	6.53e-3	1.16e-2	4.03e-3	5.20e-4
Sn_{As}	8.5	16.1	3.24	6.16	1.79	4.47e-2	2.69e-3	9.11e-4	6.86e-5
$\text{In}_{\text{As}}-\text{As}_{\text{In}}$	14.3	17.2	9.06	10.9	2.30	3.75e-2	3.68e-3	5.29e-3	5.58e-3
$\text{Ga}_{\text{As}}-\text{As}_{\text{Ga}}$	11.8	13.4	8.53	9.74	2.46	3.81e-2	4.08e-4	8.32e-5	5.66e-4

trap level positions, the Sn_{As} substitution should have a hole capture coefficient close to the double antisites. This is not the case and, additionally, despite the double antisites having near identical hole-capture coefficients, there are several orders of magnitude differences between their electron-capture coefficients. To understand the origin of the difference in capture coefficients, the main parameters behind the calculation are collected in Table II. The very low capture coefficients of the vacancies can be seen to be explained by considering the Hyang-Rhys factors of the charge states involved in the transition. The vacancies have much lower Hyang-Rhys factors than the other defects, as a consequence of their lower generalized configuration coordinate displacement. It is especially low for the more positive charge state of the transition, due to its very low phonon frequency. Similar considerations of the other Hyang-Rhys factors in Table II can explain the results in Fig. 5, if we assume a strong dependence on the Hyang-Rhys factor.

To estimate the device performance degradation associated with the investigated defects, the nonequilibrium recombination rate is calculated from the capture coefficients according to the SRH relation [29]:

$$R = \frac{np - n_i^2}{\tau_n(p + p_t) + \tau_p(n + n_t)}, \quad (8)$$

where n and p are the regular carrier densities, $n_i = p_i$ is the intrinsic carrier density, n_t and p_t are the carrier densities when the quasi Fermi level aligns with the trap level, and τ_n and τ_p are the single-electron and hole lifetimes. These lifetimes can be calculated from the capture coefficients according to $\tau_{n/p} = 1/C_{e/h}N_t$, where N_t is the density of the related defect. To calculate the SRH recombination rate with Eq. (8), we use carrier densities resulting from occupations with an electric field Fermi shift across the defect-free $\text{In}_{0.53}\text{Ga}_{0.47}\text{As}$ structure. We used the capture coefficients from Fig. 5 at a temperature of 300 K, a trap density of $N_t = 1 \times 10^{14} \text{ cm}^{-3}$ and we applied the field along the [1 1 1] direction. The resulting recombination rate is shown in Fig. 6, as a function of the applied voltage and the related excess carrier densities. Due to SRH recombination requiring both electron- and hole-capture processes to take place, in order for recombination to occur, the SRH recombination rate is dominated by the minority process. For a doped semiconductor,

this is the minority carrier capture process for most defects, which can be seen in Eq. (8) when $n \gg n_t$ and $\tau_p n \gg \tau_n p$. However, for an intrinsic semiconductor, like the one investigated in this study, the minority process depends on the defect. For example, the highest recombination rate we see in Fig. 6 is in the $\text{In}_{\text{As}}-\text{As}_{\text{In}}$ double antisite. This defect has an identical hole-capture coefficient with the $\text{Ga}_{\text{As}}-\text{As}_{\text{Ga}}$ double antisite, but the minor electron-capture coefficient is several orders of magnitude larger, yielding a much larger SRH recombination rate. Interestingly, we see that the tin substitution Sn_{As} has a larger recombination rate than the As_{Ga} antisite, despite having a smaller minor (hole-) capture coefficient. This is so because in the case of the tin substitution, the minor (hole) process and the major (electron) process have a similar capture coefficient, making them both significant in the recombination rate. Additionally, because of the density of states, the hole densities are larger than the electron densities, when the semiconductor is under a bias, which increases the impact of the electron-capture coefficient.

The recombination rate given by Eq. (8) only takes a single transition level into account, which has been sufficient for the majority of the defects studied in this paper, as they only exhibit a single local single-particle defect state.

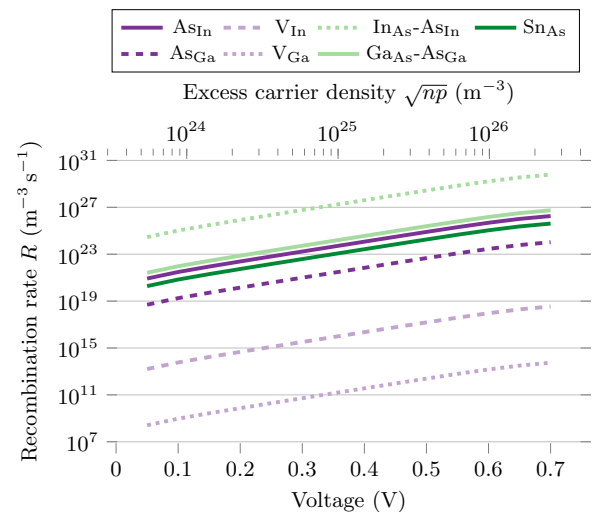


FIG. 6. Shockley-Read-Hall recombination rate for deep trap levels of point defects in $\text{In}_{0.53}\text{Ga}_{0.47}\text{As}$.

TABLE III. Transition levels of the As_{In} antisite defect in the SQS $\text{In}_{0.53}\text{Ga}_{0.47}\text{As}$ supercells consisting of $5 \times 5 \times 5$ and $6 \times 6 \times 6$ repetitions of the simple unit cell. The given formation energy is the formation energy of the stable charge state at the chemical potential of the intrinsic neutral bulk.

Transition (eV)	$5 \times 5 \times 5$ SQS supercell					$6 \times 6 \times 6$ SQS supercell				
	Low	Medium	High	Mean	STD	Low	Medium	High	Mean	STD
+3/+2	-0.3227	-0.3347	-0.3388	-0.3320	0.0068	-0.2614	-0.2490	-0.2436	-0.2513	0.0074
+2/+1	0.3634	0.4457	0.3824	0.3972	0.0352	0.4286	0.4317	0.3975	0.4193	0.0155
+1/0	0.5683	0.6564	0.5831	0.6026	0.0385	0.6457	0.6153	0.6141	0.6250	0.0146
0/-1	1.4546	1.4099	1.4012	1.4219	0.0234	1.3293	1.3309	1.3715	1.3439	0.0195
E_f (eV)	2.2160	2.0600	2.1192	2.1317	0.0643	2.0963	2.0465	2.1664	2.1031	0.0492

However, for the studied vacancies, multiple local single-particle defect states exist, corresponding to the multiple midgap transition levels. A generalization of Eq. (8), which accounts for multiple trap levels, is considered in Ref. [48]. The inclusion of multiple trap levels in the calculation of the SRH recombination has the effect of drastically reducing the SRH rate because the defects get stuck in the uppermost or lowermost charge states. But by also allowing capture into the excited states of the defect, the SRH rate is drastically increased again, balancing out the reduction. For the purpose of this paper, such an investigation was deemed out of scope, but for future studies it could be interesting to investigate how the SRH rate is impacted by such multilevel mechanisms.

VI. CONCLUSION

We have found that of the defects in $\text{In}_{0.53}\text{Ga}_{0.47}\text{As}$ studied in this paper, the defect exhibiting the highest SRH recombination rate in the intrinsic semiconductor is the $\text{In}_{\text{As}}\text{-As}_{\text{In}}$ double antisite. The remaining important defects, in descending order of recombination rate, are the $\text{Ga}_{\text{As}}\text{-As}_{\text{Ga}}$ double antisite, the As_{In} antisite, the Sn_{As} substitution, and the As_{Ga} antisite. The tin substitutions' formation energies show a favoring of the group III sites, meaning that the Sn_{As} substitution is likely only important for very high doping

levels. According to the calculated formation energies, the most stable intrinsic defects were found to be the $\text{As}_{\text{In}/\text{Ga}}$ antisites, which are in agreement with experimentally measured transition levels. While already significant in intrinsic $\text{In}_{0.53}\text{Ga}_{0.47}\text{As}$, their recombination rate should be even more detrimental in p -type $\text{In}_{0.53}\text{Ga}_{0.47}\text{As}$, owing to their high electron-capture coefficients. Similarly, due to their high hole-capture coefficients, the double antisites should be even more detrimental in n -type $\text{In}_{0.53}\text{Ga}_{0.47}\text{As}$. While not as energetically favorable as the regular antisites, the double antisites could still appear through energetically favorable combining events of singular antisites, which would lead to a strongly reduced device performance as a consequence.

ACKNOWLEDGMENT

This project has received funding from the European Union's Horizon 2020 research and innovation program under Grant Agreement No. 860095 MSCAITN-EID DESIGN-EID.

APPENDIX: TRANSITION LEVEL SQS VALIDATION DATA

Table III contains the data plotted in Fig. 3, as well as the data on the calculated transition levels which fall outside of the band gap. The formation energies of the defect in its stable charge state are also shown.

- [1] J. A. del Alamo, D. A. Antoniadis, J. Lin, W. Lu, A. Vardi, and X. Zhao, in *Proceedings of the 2015 IEEE Compound Semiconductor Integrated Circuit Symposium (CSICS)* (IEEE, Piscataway, NJ, 2015), pp. 1–4.
- [2] J. A. del Alamo, *Nature (London)* **479**, 317 (2011).
- [3] M. Heyns, *MRS Bull.* **34**, 485 (2009).
- [4] T. Skotnicki and F. Boeuf, in *Proceedings of the 2010 Symposium on VLSI Technology* (IEEE, Piscataway, NJ, 2010), pp. 153–154.
- [5] P. Ong and L. Teugels, in *Proceedings of the Advances in Chemical Mechanical Planarization (CMP)*, edited by S. Babu (Woodhead Publishing, Cambridge, 2016), pp. 119–135.
- [6] C. Convertino, C. Zota, H. Schmid, D. Caimi, M. Sousa, K. Moselund, and L. Czornomaz, *Materials* **12**, 87 (2019).
- [7] I. Vurgaftman, J. R. Meyer, and L. R. Ram-Mohan, *J. Appl. Phys.* **89**, 5815 (2001).
- [8] I. Vurgaftman and J. R. Meyer, *J. Appl. Phys.* **94**, 3675 (2003).
- [9] S. Mokkalapati and C. Jagadish, *Mater. Today* **12**, 22 (2009).
- [10] H. Zhao, P. Miao, M. Teimourpour, S. Malzard, R. Elganainy, H. Schomerus, and L. Feng, *Nat. Commun.* **9**, 981 (2018).
- [11] P. Staudinger, S. Mauthe, N. V. Triviño, S. Reidt, K. E. Moselund, and H. Schmid, *Nanotechnology* **32**, 075605 (2021).
- [12] G. Stillman, V. Robbins, and N. Tabatabaie, *IEEE Trans. Electron Devices* **31**, 1643 (1984).
- [13] G. E. Stillman, C. M. Wolfe, A. G. Foyt, and W. T. Lindley, *Appl. Phys. Lett.* **24**, 8 (1974).
- [14] B. Grandidier, H. Chen, R. M. Feenstra, D. T. McInturff, P. W. Juodawlakis, and S. E. Ralph, *Appl. Phys. Lett.* **74**, 1439 (1999).
- [15] H. Künzel, J. Böttcher, R. Gibis, and G. Urmann, *Appl. Phys. Lett.* **61**, 1347 (1992).

- [16] Y. Hwang, R. Engel-Herbert, N. G. Rudawski, and S. Stemmer, *Appl. Phys. Lett.* **96**, 102910 (2010).
- [17] H. Lee, Y. Cho, S. Jeon, and M. Shin, *IEEE Trans. Electron Devices* **68**, 5901 (2021).
- [18] N. Tajik, Z. Peng, P. Kuyanov, and R. R. LaPierre, *Nanotechnology* **22**, 225402 (2011).
- [19] L. Zhou, X. Gao, Y. Wang, L. Xu, B. Jia, D. Bai, and B. Bo, *J. Lightwave Technol.* **31**, 2279 (2013).
- [20] M.-K. Lee and C.-F. Yen, *Jpn. J. Appl. Phys.* **53**, 056502 (2014).
- [21] J. Robertson, Y. Guo, and L. Lin, *J. Appl. Phys.* **117**, 112806 (2015).
- [22] L. Zhou, B. Bo, X. Yan, C. Wang, Y. Chi, and X. Yang, *Crystals* **8**, 226 (2018).
- [23] W. Melitz, E. Chagarov, T. Kent, R. Droopad, J. Ahn, R. Long, P. C. McIntyre, and A. C. Kummel, in *Proceedings of the 2012 International Electron Devices Meeting* (IEEE, Piscat, NJ, 2012), pp. 32.4.1–32.4.4.
- [24] H.-P. Komsa and A. Pasquarello, *J. Phys.: Condens. Matter* **24**, 045801 (2012).
- [25] H.-P. Komsa and A. Pasquarello, *Phys. B (Amsterdam)* **407**, 2833 (2012).
- [26] G. Brammertz, H. Lin, K. Martens, A.-R. Alian, C. Merckling, J. Penaud, D. Kohen, W.-E. Wang, S. Sioncke, A. Delabie, M. Meuris, M. R. Caymax, and M. Heyns, *ECS Trans.* **19**, 375 (2009).
- [27] E. O'Connor, B. Brennan, V. Djara, K. Cherkaoui, S. Monaghan, S. B. Newcomb, R. Contreras, M. Milojevic, G. Hughes, M. E. Pemble, R. M. Wallace, and P. K. Hurley, *J. Appl. Phys.* **109**, 024101 (2011).
- [28] T. K. Oanh Vu, M. T. Tran, N. X. Tu, N. T. Thanh Bao, and E. K. Kim, *J. Mater. Res. Technol.* **19**, 2742 (2022).
- [29] W. Shockley and W. T. Read, *Phys. Rev.* **87**, 835 (1952).
- [30] S. Smidstrup, T. Markussen, P. Vancaerayveld, J. Wellendorff, J. Schneider, T. Gunst, B. Verstichel, D. Stradi, P. A. Khomyakov, U. G. Vej-Hansen, M.-E. Lee, S. T. Chill, F. Rasmussen, G. Penazzi, F. Corsetti, A. Ojanperä, K. Jensen, M. L. N. Palsgaard, U. Martinez, A. Blom *et al.*, *J. Phys.: Condens. Matter* **32**, 015901 (2020).
- [31] M. van Setten, M. Giantomassi, E. Bousquet, M. Verstraete, D. Hamann, X. Gonze, and G.-M. Rignanese, *Comput. Phys. Commun.* **226**, 39 (2018).
- [32] J. Heyd, G. E. Scuseria, and M. Ernzerhof, *J. Chem. Phys.* **118**, 8207 (2003).
- [33] J. P. Perdew, K. Burke, and M. Ernzerhof, *Phys. Rev. Lett.* **77**, 3865 (1996).
- [34] H.-P. Komsa and A. Pasquarello, *Appl. Phys. Lett.* **97**, 191901 (2010).
- [35] P. Śpiewak and K. J. Kurzydłowski, *Phys. Rev. B* **88**, 195204 (2013).
- [36] M. Guidon, J. Hutter, and J. Van de Vondele, *J. Chem. Theory Comput.* **6**, 2348 (2010).
- [37] C. Freysoldt, J. Neugebauer, and C. G. Van de Walle, *Phys. Rev. Lett.* **102**, 016402 (2009).
- [38] C. Freysoldt, B. Grabowski, T. Hickel, J. Neugebauer, G. Kresse, A. Janotti, and C. G. Van de Walle, *Rev. Mod. Phys.* **86**, 253 (2014).
- [39] S. E. Taylor and F. Bruneval, *Phys. Rev. B* **84**, 075155 (2011).
- [40] A. van de Walle, P. Tiwary, M. de Jong, D. Olmsted, M. Asta, A. Dick, D. Shin, Y. Wang, L.-Q. Chen, and Z.-K. Liu, *Calphad* **42**, 13 (2013).
- [41] K. Goetz, D. Bimberg, H. Jürgensen, J. Selders, A. V. Solomonov, G. F. Glinskii, and M. Razeghi, *J. Appl. Phys.* **54**, 4543 (1983).
- [42] J. Robertson and L. Lin, *Appl. Phys. Lett.* **99**, 222906 (2011).
- [43] D. Cui, S. M. Hubbard, D. Pavlidis, A. Eisenbach, and C. Chelli, *Semicond. Sci. Technol.* **17**, 503 (2002).
- [44] A. Alkauskas, Q. Yan, and C. G. Van de Walle, *Phys. Rev. B* **90**, 075202 (2014).
- [45] A. Alkauskas, J. L. Lyons, D. Steiauf, and C. G. Van de Walle, *Phys. Rev. Lett.* **109**, 267401 (2012).
- [46] M. E. Turiansky, A. Alkauskas, M. Engel, G. Kresse, D. Wickramaratne, J.-X. Shen, C. E. Dreyer, and C. G. Van de Walle, *Comput. Phys. Commun.* **267**, 108056 (2021).
- [47] R. Pässler, *Phys. Status Solidi B* **78**, 625 (1976).
- [48] A. Alkauskas, C. E. Dreyer, J. L. Lyons, and C. G. Van de Walle, *Phys. Rev. B* **93**, 201304(R) (2016).